Improvements to the LAURA Mesh Adaptation Algorithm

Kyle B. Thompson*, Adam J. Wise†, Brian R. Hollis‡ and Andrew D. Hinkle§
NASA Langley Research Center,
Hampton, VA 23681, USA

This paper describes recent improvements to the LAURA code that removes the requirement of unbroken body-normal lines when using the automated mesh adaptation algorithm in LAURA responsible for mesh alignment with shock and adjusting near-wall mesh spacing. For a complex geometry, restricting block topologies such that blocks span the domain from the surface wall boundaries to domain outer boundary can be difficult or impossible. Removing this requirement enables novel block topologies that simplify the meshing workflow for LAURA users. The new adaptation algorithm implementation in LAURA is described and several examples of the adaptation are presented to demonstrate the efficacy of the adaptation algorithm.

I. Introduction

To improve the accuracy of aerothermal predictions in hypersonic flow conditions with strong shocks, the LAURA code [1] uses an r-adaptation algorithm to align the multiblock structured mesh with the vehicle bow shock and adjusts the near wall spacing to sufficiently resolve the boundary layer. This algorithm has been effectively used to improve the accuracy of surface heat transfer predictions as well as stabilize the nonlinear solver during iterative convergence to steady state; however, it relies upon a convention that grid lines in the structured mesh are adapted only if they span from the vehicle surface to the domain outer boundary. This convention restricts the block topologies that can be used during mesh generation, prohibiting meshing techiques that would otherwise be used on relatively complex vehicle geometries.

A recent and relevant example of complex vehicle geometry that requires block topologies breaking the standard LAURA adaptation convention is the Low-Earth Orbit Flight Test of an Inflatable Decelerator (LOFTID) [2, 3]. Figure 1 shows an example block topology for a simplified axisymmetric geometry definition of the LOFTID vehicle. Because

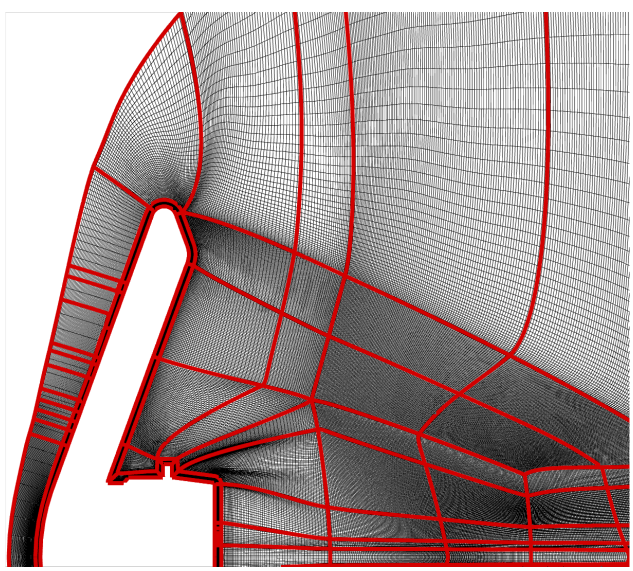

Fig. 1 Example Block Topology Breaking LAURA Adaptation Convention.

*Aerospace Engineer, Aerothermodynamics Branch, Member AIAA.
†Aerospace Engineer, Aerothermodynamics Branch, Member AIAA.
‡Senior Technical Lead for Planetary Entry Systems, Aerothermodynamics Branch, Associate Fellow AIAA.
§Aerospace Engineer, Aerothermodynamics Branch, Member AIAA.

LAURA requires full matching of block-to-block faces, this block topology is required to construct a multiblock, structured mesh around key geometric details on the aft section of the vehicle. The conventional LAURA r-adaptation algorithm cannot be used here due to body-normal k-lines that do not span the distance between the vehicle surface and the outer boundary of the structured mesh. Accurate heat transfer predictions are important in the aft section of the vehicle, because the vehicle has a minimal thermal protection system (TPS) there. This work demonstrates an improvement to the LAURA mesh adaptation algorithm that removes the restriction on continuous grid lines, allowing mesh adaptation for this type of block topology.

II. LAURA CFD Flow Solver

LAURA is a multiblock structured grid finite-volume CFD solver developed at the NASA Langley Research Center. LAURA has been used for aerothermal analysis support of the entry, descent and landing (EDL) phase of interplanetary missions over the last three decades [4–6]. The code solves the reacting flow equations with support for high-energy physics, including thermal and chemical nonequilibrium modeling, surface catalysis and ablation. The LAURA software package includes the HARA code [7], which enables a coupled radiation capability for radiative heat transfer predictions, and hybrid continuum-rarified simulation capability is possible through a post-processing coupling step using the MAP DSMC code [8].

III. Mesh Adaptation Algorithm

The LAURA mesh adaptation algorithm focuses on two details:

- aligning the domain outer boundary with the bow shock.
- adjusting the near-wall mesh spacing.

The alignment of the outer domain to the shock is critical for accurate heat transfer predictions, because it minimizes the dissipation applied by the STVD flux function [9]. Without alignment, the shock capturing scheme used by LAURA is overly dissipative, resulting in distorted surface heat transfer predictions. Ensuring that the near-wall spacing is sufficiently small to resolve the thin boundary layer commonly seen in hypersonic applications is equally important for accurate surface heat transfer predictions. Figure 2 shows the effect of mesh realignment on the surface heat flux for a hemisphere simulation. Without alignment, the surface heat flux is overpredicted and distorted, with the shock poorly

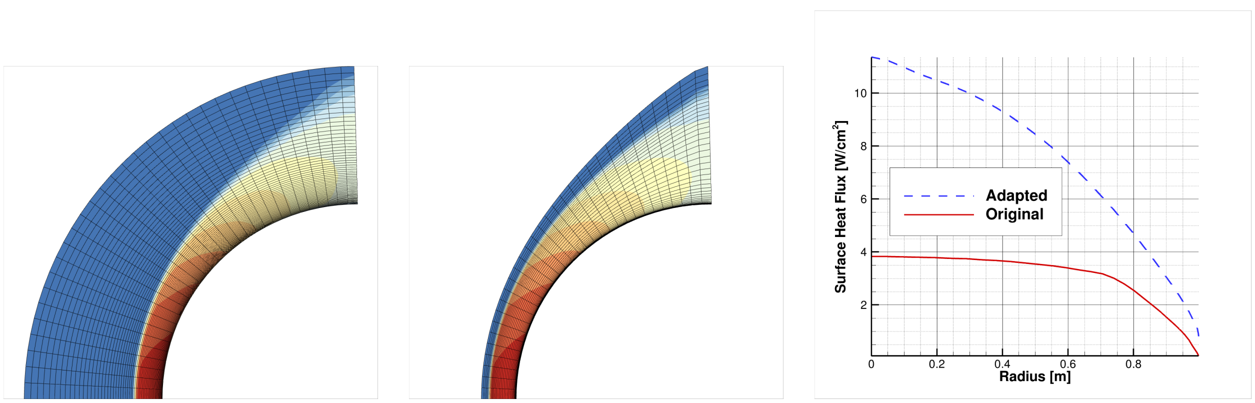

(a) Original **(b) Adapted** **(c) Convective Heat Flux**

Fig. 2 Hemisphere temperature contours and heat flux before and after adaptation.

captured over multiple cells. After alignment, the shock is captured within 3 cells and the surface heat flux accuracy improves.

The standard mesh adaptation algorithm used in LAURA assumes unbroken grid lines in the k-index direction. Using this convention, each k-direction line is represented as a parameterized piecewise-linear function. To simplify mesh generation by removing the requirement of unbroken k-direction lines, a new algorithm is implemented in LAURA based on the user-specied boundary conditions assigned to each block face. Blocks in the mesh fall in four catagories:

1) Blocks with a single block face assigned a solid surface boundary condition

2) Blocks with a single block face assigned a freestream (i.e., inflow) boundary condition
3) Blocks with a single block face assigned a solid surface boundary condition and the opposite block face assigned a freestream boundary condition (i.e., the standard LAURA adaptation convention)
4) All other blocks not satisfying the previous three conditions

Examples of these block types are highlighted in red in Figure 3. Type-1 blocks (Figure 3a) must be adapted such that

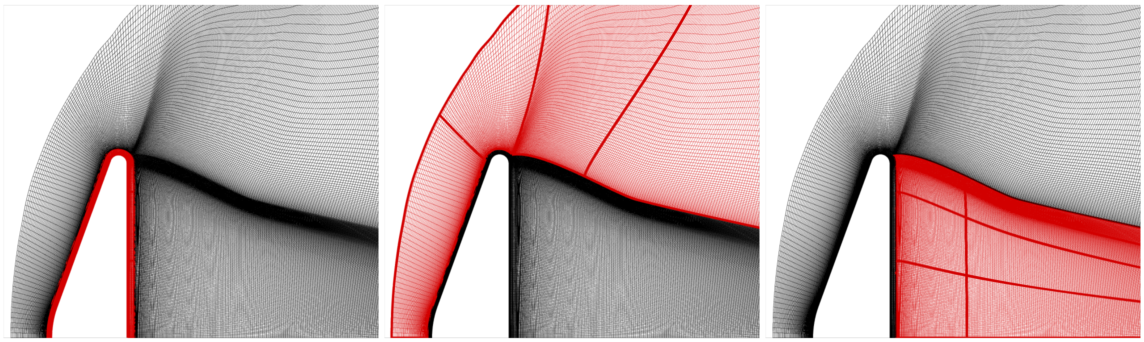

(a) Type-1 Block **(b) Type-2 Block** **(c) Type-4 Block**

Fig. 3 Adaptation Block Type Examples.

the near-wall spacing is sufficiently small enough to spatially resolve the boundary layer. Type-2 blocks (Figure 3b) must adapt the outer domain such that the mesh is aligned with a shock wave captured with the block. Type-3 blocks, such as the example in Figure 2, are adapted using the standard LAURA mesh adaptation algorithm. No adaptation is performed on type-4 blocks (Figure 3c).

A. Near-wall Adaptation Algorithm

To resolve flow near solid surfaces, points along wall-normal lines are redistributed according to the two-sided stretching function of Vinokur [10]

$$\eta = \frac{u}{A + (1 - A)u} \tag{1}$$

$$u = \begin{cases} \frac{1}{2} + \frac{\tanh[\Delta y(k_i - 1/2)]}{2\tanh(\Delta y/2)}, & B > 1.001 \\ \frac{1}{2} + \frac{\tan[\Delta y(k_i - 1/2)]}{2\tan(\Delta y/2)}, & B < 0.999 \\ \Delta y \left[1 - 2\Delta y(B-1)(\Delta y - \frac{1}{2})\right], & \text{else} \end{cases} \tag{2}$$

$$k_i = \frac{i}{N_{\text{points}} - 1}, \quad A = \sqrt{s_0/s_1}, \quad B = \sqrt{s_0 s_1} \tag{3}$$

where η is normalized arc length, s_0 is the initial slope of the stretching function, s_1 is the final slope of the stretching function, and Δy is computed from the approximate analytic representation of inverse functions described in Ref. [10]. The slopes, s_0 and s_1, are computed using a Newton iteration such that the initial and final spacings of the distribution match prescribed target values. The initial spacing (i.e., cell height of the initial cell off the wall), h_w is determined such that the cell Reynolds number of all cells at the wall are less than some user-specified value. The cell Reynolds number is computed as

$$Re_c = \frac{\max(\rho_\infty/2, \rho) a h_w}{\mu}, \tag{4}$$

where ρ is the density in the cell, ρ_∞ is the freestream density, a is speed of sound in the cell, and μ is the viscosity in the cell. The spacing at the upper bound of the distribution is set to match the spacing prescribed in the initial mesh point distribution. This is done so that the block-to-block spacing intentionally set by the user is left intact and so that point redistribution is independent of the changes made during previous point redistributions.

B. Shock Alignment Algorithm

To align the structured mesh outer boundary with a strong bow shock, the points along lines orthogonal to the outer boundary are redistributed. The redistribution of points follow a geometric growth rate

$$\eta_i = g(\eta_{i-1} - \eta_{i-2}) + \eta_{i-1}, \tag{5}$$

where η_i is the arc length at point i and g is the growth rate. A Newton iteration is used to determine the growth rate needed to match a target total arc length based on the initial arc length, η_1. As with the near-wall spacing function, the spacing at the end of the distribution that adjoins another block is left unchanged from what was prescribed in the initial mesh. To align the outer boundary with the shock, the total arc length of each line is scaled such that the detected shock location would reside at some target arc length, η_{target}, of the newly rescaled line. The shock location is detected by marching from the outer boundary until the jump between solution values exceeds some threshold. In LAURA, the user can choose between density, pressure, and temperature as the solution value to use in shock detection. The shock location arc length, η_s, is then used to compute the line scaling factor

$$S = \frac{\eta_s}{\eta_{\text{target}}}, \tag{6}$$

with points extrapolated based on the final line segment direction when $S > 1$.

When the shock is poorly captured due to misalignment with the mesh, the scaling factors can be nonsmooth. This results in "kinks" in the outer domain, which creates problems for future mesh adaptation cycles. To mitigate the issue of nonsmoothness in the scale factors of adjacent lines, Taubin smoothing [11] is applied to the scaling factor field. Figure 4 shows a close-up cross section view of a shock alignment adaptation with and without Taubin smoothing applied to the scaling factors of each line length. Without any smoothing, outer boundary normals are oscillatory, whereas the application of Taubin smoothing results in a much cleaner adapted mesh.

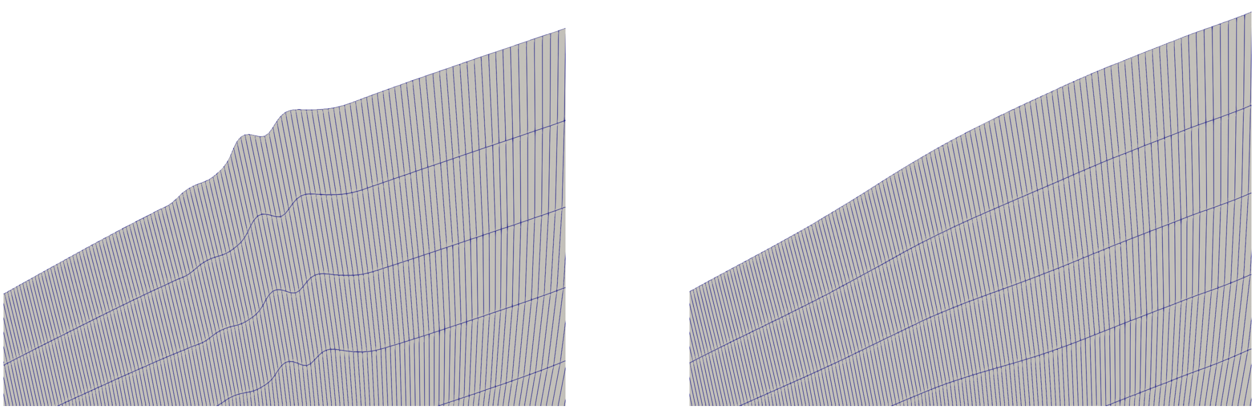

(a) Without Taubin Smoothing **(b) With Taubin Smoothing**

Fig. 4 Effect of Taubin smoothing on adaptation of domain outer boundary.

C. Correcting skewness resulting from irregular initial cell height

The stacked block topology adaptation algorithm was employed to simulate the aerothermal environment for the Mars 2020 vehicle [12]. During the course of adaptation, spacing irregularities resulting in high cell skewness were observed near block boundaries. Figure 5 shows an example of the these irregularities, and the cause was determined to be a limitation of the geometric growth function used in the shock-mesh alignment. As mentioned before, a requirement of the adaptation algorithm is that the block-to-block spacing should be preserved, meaning the initial cell height at the base of lines orthogonal to the domain boundary is left unchanged. Because the growth rate in the distribution function used in these blocks is strongly dependent on the initial cell spacing, irregularity in the initial cell spacing in neighboring lines will result in the type of skewness observed in Figure 5b. Figure 5c shows an example of this type of initial cell spacing, which is common near geometric singularities in meshes generated using elliptic PDE or variational grid smoothing techniques.

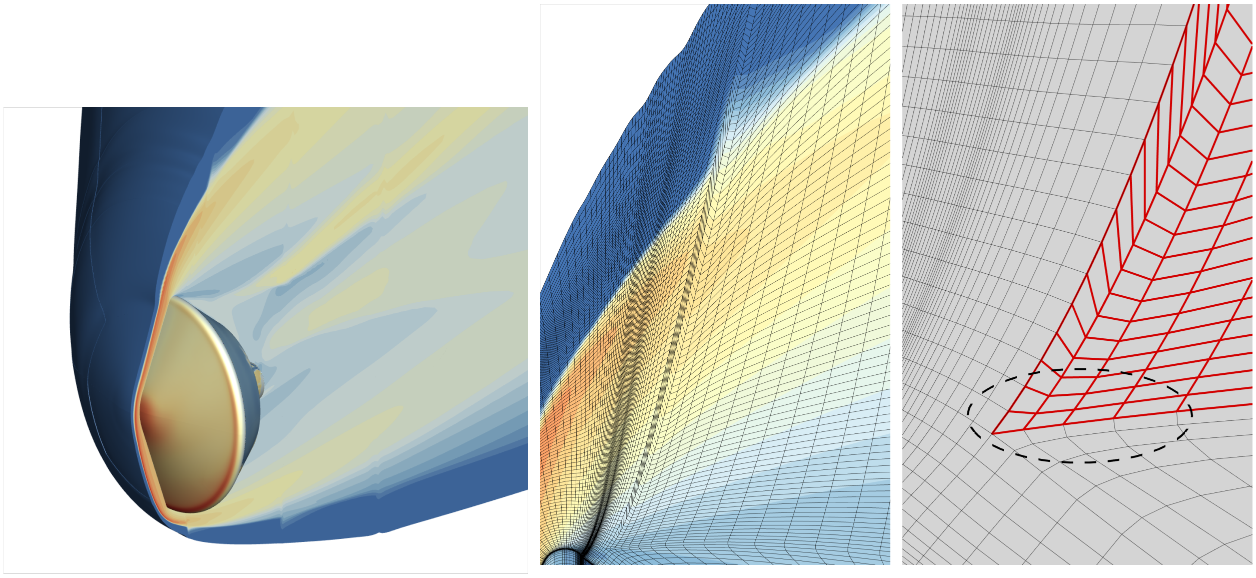

(a) Temperature and Surface Heat Flux. (b) Distribution Function Failure. (c) Irregular Initial Spacing.

Fig. 5 Mars 2020 vehicle with stacked block adapted mesh.

This limitation of the adaptation algorithm can be alleviated by enforcing smoothly varying or constant initial cell spacing. To minimize the effect of irregular initial spacings on the distribution function while still allowing for variation across the block, the initial spacing used to build the distribution function is bilinearly interpolated from the initial spacing of the block's corner points. The initial spacing, u_0, used in the geometric distribution function is found as follows:

$$u_0 = [(1-\xi)(1-\eta)]\, u_{i_{\min} j_{\min}} + [\xi\ (1-\eta)]\, u_{i_{\min} j_{\max}} + [(1-\xi)\ \eta]\, u_{i_{\max} j_{\min}} + [\xi\ \eta]\, u_{i_{\max} j_{\max}} \quad (7)$$

where $u_{i_{\min} j_{\min}}$, $u_{i_{\min} j_{\max}}$, $u_{i_{\max} j_{\min}}$, and $u_{i_{\max} j_{\max}}$ are the initial cell height spacings at the respective corners of the block, ξ is the fraction of arc length in the grid i-index direction, and η is the fraction of arc length in the grid j-index direction. to avoid issues with reversibility of the adaptation process, the corrected initial spacing, u_0, is reverted to original spacing in the mesh after the geometric distribution is applied along the line. Figure 6 shows the comparison of adaptation applied with and without the bilinear interpolation correction on the initial cell height. Without the correction, the k-line distributions near the block boundary result in kinked grid lines. The correction results in better grid and solution quality in this region.

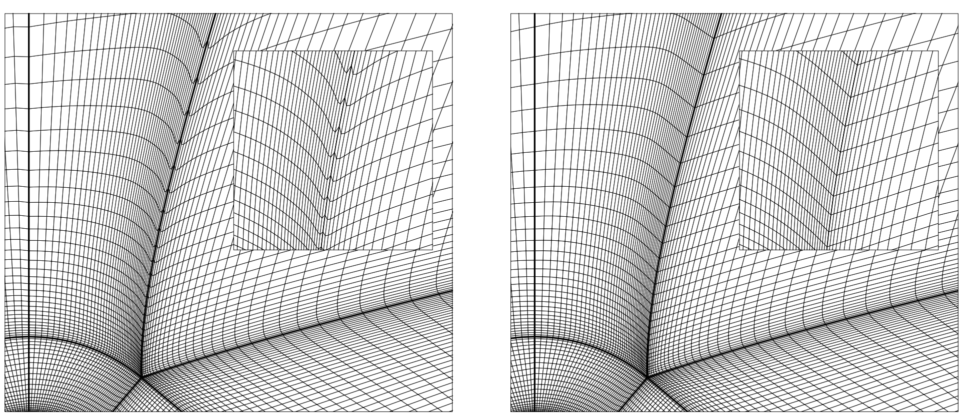

(a) Original. (b) Corrected.

Fig. 6 Skewness correction via bilinear interpolation of initial spacing.

IV. Results

A series of cases are presented to demonstrate the effectiveness of the new adaptation algorithm.

A. Axisymmetric Case: AGARD Working Group 18 Wind Tunnel Model

The AGARD Working Group 18 model [13, 14] is a 70-degree capsule wind tunnel model. Figure 7 shows a comparison of two mesh configurations for this case: one using the new adaptation algorithm with a novel block topology and one using the conventional topology of body-normal lines spanning the domain. Figure 7b shows that the

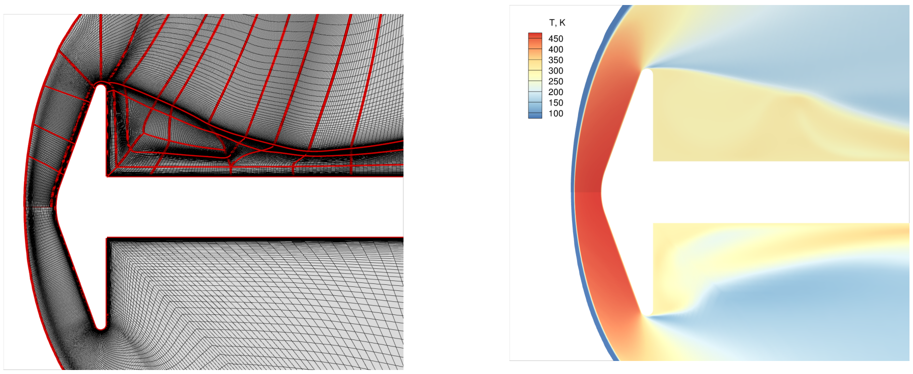

(a) Mesh block topology. **(b) Temperature contours.**

Fig. 7 AGARD Working Group 18 Model stacked (top) vs conventional (bottom) block topologies.

new stacked topology allows better resolution of the wake region, particularly in capturing the shear layer originating from the shoulder of the model. The new adaptation algorithm performs well on the stacked block configuration, with Figure 8 showing excellent agreement in surface heat flux on the forebody of the model. Notable differences in the

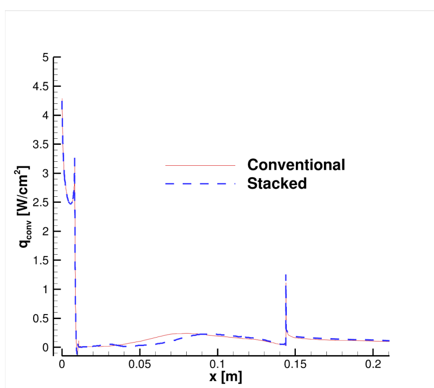

Fig. 8 AGARD Working Group 18 Model surface heat flux.

heat flux in the wake region can be explained by the improvement of mesh resolution offered by the new stacked block topology, allowing the user to carefully craft the mesh spacing in the Type-4 blocks to adequately capture flow features without influencing the upstream mesh density.

B. Three-Dimensional Case: MSL Wind Tunnel Model

The Mars Science Laboratory OML-6 configuration model [15] is a 70-degree capsule wind tunnel model with a biconic backshell geometry. Similar to the AGARD Working Group 18 model results shown in Sec. IV.A, a comparison was made between the traditional and stacked block topoologies. Figure 9 shows the temperature contours on the symmetry plane of the model at 16 degrees angle of attack using both a traditional and stacked-block topology for the MSL case. Both grids share the same surface grid point distribution, but the traditional grid was generated by a standard hyperbolic extrusion approach. The clustering of grid points in some regions of the wake, due to the hyperbolic grid generation process, lead to cells with large skew and spacing changes. These grid quality deficiencies make it difficult to accurately solve the flow at this region, which is evident in the wake solution in Figure 9a. It is also important to note that the skew and spacing jumps in this region for the traditional grid resulted in difficulty maintaining solution stability and required extremely conservative relaxation parameters and dual time-stepping. The stacked-block grid resulted in a much higher quality solution as shown in Figure 9b, as well as a much faster time to solution due to the solver's ability to evolve the solution easier with high quality grid point distribution. While not all traditional grids may experience robustness issues like in this case, a stacked-block grid allows for more control of the grid quality throughout the domain and overall solution quality.

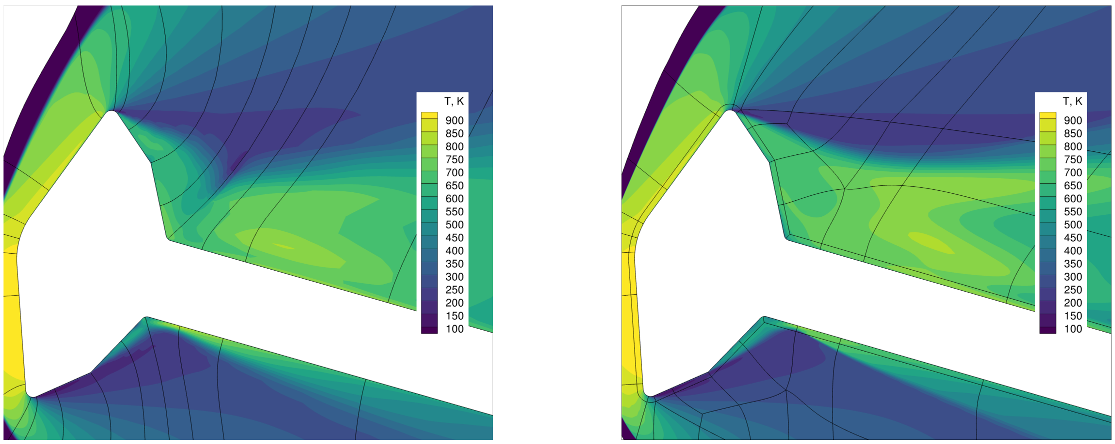

(a) Traditional topology. **(b) Stacked-block topology.**

Fig. 9 MSL OML-6 wind tunnel model temperature contours.

C. Three-Dimensional Case: AGARD Working Group 18 Wind Tunnel Model

A three-dimensional mesh of the AGARD Working Group 18 model is included to demonstrate equivalent performance of the adaptation algorithm on a three dimensional geometry. Figure 10 shows temperature contours and block topology for the three-dimensional mesh, which uses the same stacked block topology as shown in Figure 7. A key difference between the axisymmetric and three-dimensional simulations is the three-dimensional relief effect. Because the axisymmetric condition constrains the flow, fluctuations in the axial direction are not possible. This supresses

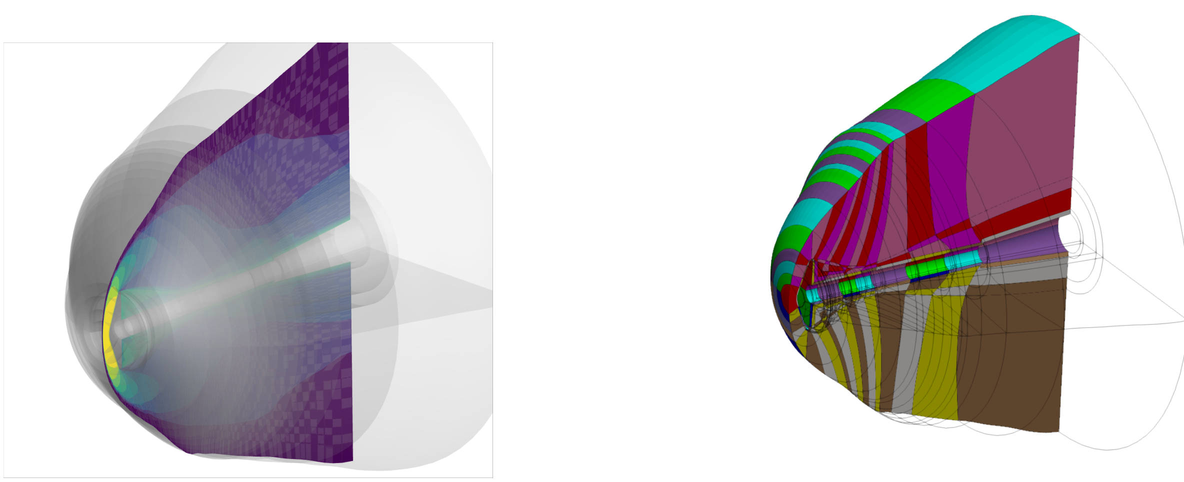

(a) Temperature contours. **(b) Block topology.**

Fig. 10 AGARD Working Group 18 Model with Stacked Block Adapted 3D Mesh.

unsteadiness in the axisymmetric simulation that would otherwise be observed in a three-dimensional simulation. This is observed in comparing the time-averaged heat flux on the model sting. Figure 11 shows excellent agreement between the axisymmetric and a Y-plane cut of the three-dimensional solutions for the forebody, but differences along the sting region are still evident. This indicates the importance of the choice of the boundary conditions for the wake flow region, where an axisymmetry condition can distort the accuracy of the wake region results.

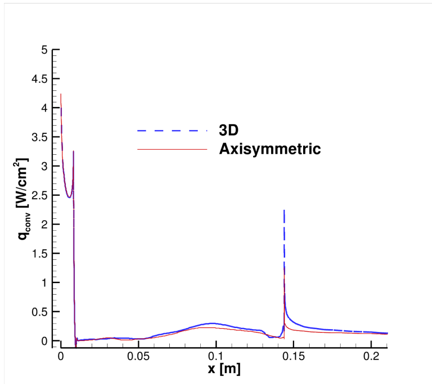

Fig. 11 AGARD Working Group 18 Model 3D vs axisymmetric surface heat flux.

D. Three-Dimensional Case: LOFTID Wind Tunnel Model

The Low-earth Orbit Flight Test of an Inflatable Decelerator (LOFTID) demonstrated the use of an inflatable aerodynamic decelerator at operational mission relevant conditions in 2022. Prior to the flight test, extensive simulations were performed to define the vehicles aerothermodynamic flight environments. Wind tunnel tests were conducted to obtain experimental heat-transfer data for comparison with the predictions to help define computational uncertainty margins. A photograph of a LOFTID wind tunnel model is shown in Figure 12a along with the stacked-block computational mesh topology in Figure 12b. In addition to the complexities of wake flow meshing described previously, the LOFTID geometry added the challenge of resolving the flow field over the exposed inflation toroids on the back of the vehicle.

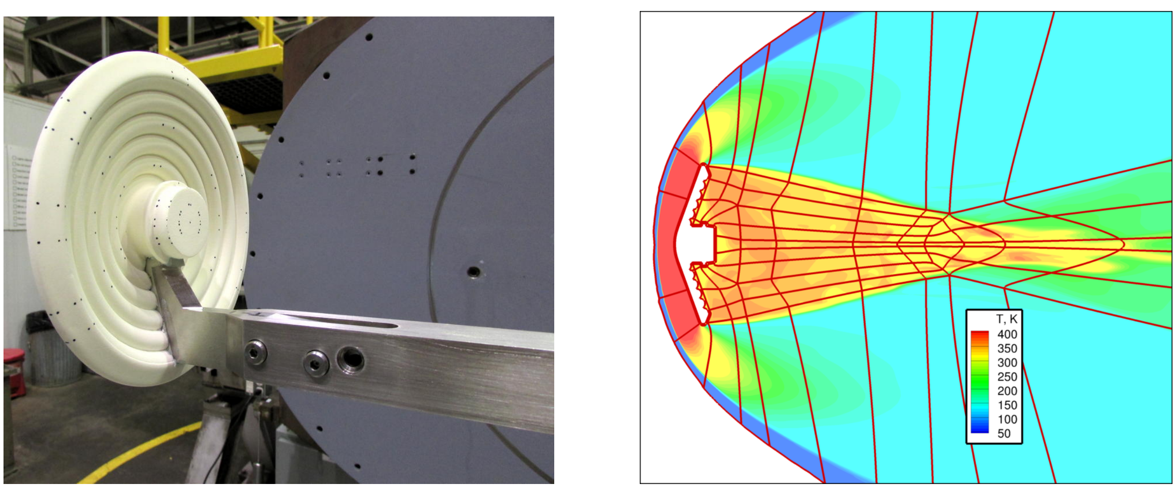

(a) Wind tunnel model [Source: NASA]. **(b) Block topology and temperature contours.**

Fig. 12 LOFTID wind tunnel model and associated structured grid block topology.

Aeroheating data were obtained using global phosphor thermography [16] in the 31-Inch Mach 10 Air Tunnel [17] of the NASA Langley Aerothermodynamic Laboratory (LAL). These data were compared with LAURA simulations at the test conditions using first-order time-stepping on a three-dimensional, stacked-block mesh topology. Surface heating predictions were time averaged to obtain distributions for comparisons with the experimental data and results are shown in Figure 13a and Figure 13b. The uncertainty in the experimental data - on the order of 25% - is higher than typical studies due to the difficulty in measuring the very small surface temperature rise (< 5K) during a wind tunnel run. The data and predictions matched to within the experimental uncertainties with the exception of some local toroid heating peaks at the highest test Reynolds numbers. These discrepancies may be due to the growth of turbulence in the separated wake shear layer, which would not have been captured by the laminar flow-field simulations.

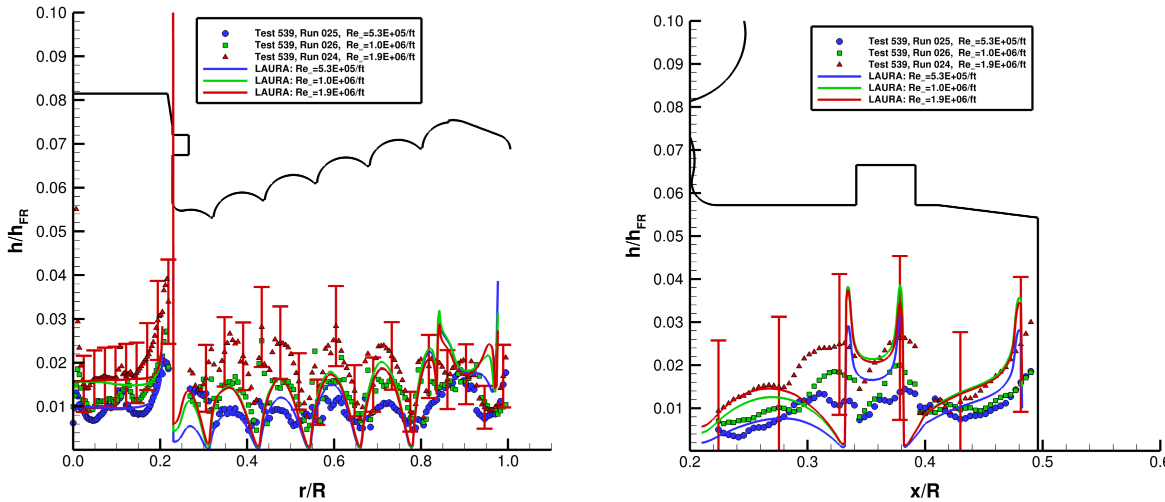

(a) Aeroshell backface. **(b) Centerbody Payload.**

Fig. 13 Comparisons of predicted and measured heating distributions.

V. Concluding Remarks

A mesh adaptation algorithm that does not require unbroken grid lines spanning the domain is presented. The adaptation algorithm is demonstrated to be robust and effective for enabling finer-grained control over mesh spacing on vehicle geometries representative of Entry, Descent and Landing applications. Additionally, by separating the adaptation of shock-mesh alignment and near-wall spacing, the total mesh density in the wake region can be decoupled from the forebody region, which is not easily achieve with the original LAURA constraint of unbroken body-normal grid lines. The adaptation algorithm has some drawbacks, particularly in regard to the requirement of near-uniform spacing near some block boundaries; however, the expectation is that these drawbacks are outweighed by the flexibility afforded by this type of multiblock structured mesh generation. Ultimately, this work represents a meaningful way to achieve better mesh resolution and fidelity for LAURA simulations of a complex geometry.

VI. Acknowledgements

The authors would like to thank the Entry Systems Modeling Project within the NASA Game Changing Development Program, Space Technology Mission Directorate for their funding and support of this research.

References

[1] Thompson, K. B., Hollis, B. R., Johnston, C. O., Kleb, B., Lessard, V. R., and Mazaheri, A., "LAURA Users Manual: 5.6," NASA TM-2020-220566, Langley Research Center, 2020.

[2] Swanson, G., Kazemba, C., Hughes, S., Williams, J., Johnson, K., Mike, Lindell, Bodkin, R., DiNonno, J., and Cheatwood, N., "Low-Earth Orbit Flight Test of an Inflatable Decelerator (LOFTID) – Aeroshell Engineering Development Unit Structural Testing," *16th International Planetary Probe Workshop*, 2019.

[3] Reed, J. G., Holguin, M., Cheatwood, F. M., and DiNonno, J. M., "Vulcan Centaur Reuse," AIAA Paper 2020-4122, 2020.

[4] Braun, R. D., Powell, R. W., Engelund, W. C., Gnoffo, P. A., Weilmuenster, K. J., and Mitcheltree, R. A., "Mars Pathfinder six-degree-of-freedom entry analysis," *Journal of Spacecraft and Rockets*, Vol. 32, No. 6, 1995, pp. 993–1000.

[5] Hash, D., Olejniczak, J., Wright, M., Prabhu, D., Pulsonetti, M., Hollis, B., Gnoffo, P., Barnhardt, M., Nompelis, I., and Candler, G., "FIRE II Calculations for Hypersonic Nonequilibrium Aerothermodynamics Code Verification: DPLR, LAURA, and US3D," AIAA Paper 2007-605, 2007.

[6] Johnston, C. O., West, T. K., and Brandis, A. M., "Features of Afterbody Radiative Heating for Titan Entry," AIAA Paper 2019-3010, 2019.

[7] Johnston, C. O., "Nonequilibrium Shock-Layer Radiative Heating for Earth and Titan Entry," Ph.D. thesis, Virginia Polytechnic Institute and State University, 2006.

[8] Liechty, D. S., Wise, A. J., Subramaniam, S., and Stephani, K. A., "Comparison Of CFD And DSMC Using Calibrated Transport Parameters," 2018.

[9] Yee, H. C., "On Symmetric and Upwind TVD Schemes," NASA TM-86842, 1985.

[10] Vinokur, M., "On one-dimensional stretching functions for finite-difference calculations," *Journal of Computational Physics*, Vol. 50, No. 2, 1983, pp. 215–234. doi:https://doi.org/10.1016/0021-9991(83)90065-7.

[11] Taubin, G., "Curve and surface smoothing without shrinkage," *Proceedings of IEEE International Conference on Computer Vision*, 1995, pp. 852–857. doi:10.1109/ICCV.1995.466848.

[12] Wise, A., Prabhu, D. K., Johnston, C. O., Saunders, D. A., and Edquist, K. T., "Computational Aerothermodynamic Environments for the Mars 2020 Entry Capsule," AIAA Paper 2018-3116, 2018.

[13] Horvath, T., McGinley, C., and Hannemann, K., "Blunt body near-wake flow field at Mach 6," AIAA Paper 1996-1935, 1996.

[14] Nance, R., Hassan, H., Hollis, B., and Horvath, T., "Solution of transitional wake flows at Mach 10," AIAA Paper 1998-2939, 1998.

[15] Hollis, B. R., and Collier, A. S., "Experimental Investigation of Mars Science Laboratory Entry Vehicle Aeroheating in AEDC Hypervelocity Tunnel 9," Tech. Rep. TP-2017-219658, 2017.

[16] Mason, M. L., and Rufer, S. J., "Imaging for Hypersonic Experimental Aeroheating Testing (IHEAT) version 4.0: User Manual," NASA TM-2018-220113, Langley Research Center, 2018.

[17] Berger K., H. K., Rufer S., and S., W., "NASA Langley Aerothermodynamic Laboratory: Hypersonic Testing Capabilities," AIAA Paper 2015-1337, 2015.